

High-Voltage Potassium Ion Micro-Supercapacitors with Extraordinary Volumetric Energy Density for Wearable Pressure Sensor System

Shuanghao Zheng, Jiaxin Ma, Kaixin Fang, Shiwen Li, Jieqiong Qin, Yaguang Li, Jiemin Wang, Liangzhu Zhang, Feng Zhou, Fangyan Liu, Kai Wang, and Zhong-Shuai Wu*

To cater for the rapid development of flexible, wearable and implantable microelectronics, the miniaturized and integrated energy storage devices with mechanically robust properties, high voltage, and highly compatible integration are in extreme demand. Here, potassium ion micro-supercapacitors (KIMSCs) are rationally designed by applying MXene-derived potassium titanate (KTO) nanorods anode and porous activated graphene (AG) cathode to power the sensitively integrated pressure sensing system. Benefiting from the advanced nanostructure of KTO nanorods, it offers a high potassium ion storage capacity of 145 mAh g⁻¹. Notably, the constructed KIMSCs exhibit a large operating voltage window of 3.8 V, outperforming the previously reported micro-supercapacitors. Furthermore, an extraordinary volumetric energy density of 34.1 mWh cm⁻³ is achieved for KIMSCs with robust rate capability and remarkable capacitance retention, due to the dominated capacitive mechanism and tiny volume change of reversible intercalation/deintercalation of K cations in KTO and adsorption/desorption of bis(trifluoromethanesulfonyl) imide anions on AG. More importantly, a KIMSC compatibly integrated with a wireless pressure sensor on a flexible substrate can monitor body movement. Therefore, this work not only provides insight on designing high-performance KIMSCs, but also presents a blueprint for KIMSCs powered flexible electronics.

performance and high integration.^[1–8] Among the miniaturized energy storage units, micro-supercapacitors (MSCs) hold a great potential for microelectronics, due to the ultrahigh power density, fast charge and discharge rate, and long life stability. Nevertheless, despite the intrinsically reversible adsorption of electrolyte ions or rapid Faradaic reaction, current MSCs still suffer from relatively low energy density and narrow potential window.^[9–13] To address this gap, hybrid ion MSCs (HIMSCs) have been emerging to cover the merits of both battery-type negative electrode and supercapacitor-type positive electrode, where high energy density and high power density can be simultaneously achieved.^[14–18] For instance, lithium ion MSCs as a typical kind of HIMSCs have demonstrated to possess high energy density and long cyclability.^[14,19,20] Nevertheless, the increasing cost and low crustal abundance of lithium will restrain the further development of lithium ion MSCs.^[21–23]

In contrast, substantial efforts have been devoted into potassium ion energy storage devices, owing to the abundant potassium resource in crust and comparable energy density.^[24–26] The reduction potential of potassium (–2.93 V vs SHE) gets close to that of lithium (–3.04 V vs SHE), enabling a high operating voltage of potassium ion batteries comparable to lithium ion batteries.^[27,28]

1. Introduction

The modularized and miniaturized electronics for portable and wearable devices have intensively accelerated the need for microscale electrochemical energy storage devices with robust

Dr. S. Zheng, J. Ma, K. Fang, S. Li, Dr. Y. Li, Dr. J. Wang, Dr. L. Zhang,
Dr. F. Zhou, Dr. F. Liu, Prof. Z.-S. Wu
State Key Laboratory of Catalysis
Dalian Institute of Chemical Physics
Chinese Academy of Sciences
457 Zhongshan Road, Dalian 116023, China
E-mail: wuzs@dicp.ac.cn

Dr. S. Zheng, Dr. F. Zhou, Dr. F. Liu, Prof. Z.-S. Wu
Dalian National Laboratory for Clean Energy
Chinese Academy of Sciences
457 Zhongshan Road, Dalian 116023, China

 The ORCID identification number(s) for the author(s) of this article can be found under <https://doi.org/10.1002/aenm.202003835>.

DOI: 10.1002/aenm.202003835

J. Ma, S. Li
University of Chinese Academy of Sciences
19 A Yuquan Road, Shijingshan District, Beijing 100049, China
K. Fang
School of Chemistry and Chemical Engineering
Guangxi University
No. 100 Daxue East Road, Nanning 530004, China

Dr. J. Qin
College of Science
Henan Agricultural University
No. 63 Agricultural Road, Zhengzhou 450002, China

Prof. K. Wang
Institute of Electrical Engineering
Chinese Academy of Sciences
Beijing 100190, China

Moreover, potassium ions in non-aqueous electrolyte have a weaker solvation effect and smaller Stokes' radius than lithium ions, contributing to a higher ion transfer number and conductivity.^[29] Inspired by high capacity, black phosphorous and metal chalcogenides (e.g., SnS₂, MoS₂) with conversion or alloying reaction are currently preferred for potassium ion storage.^[30–33] However, when they are applied for potassium ion MSCs (KIMSCs), the pre-intercalation or activation of K cations is usually required, which makes the volume of electrode hugely expanded and the preparation process more complex and time consuming.^[34–36] By comparison, potassium titanate (KTO) crystal structure possessing open channel and huge interstitial space is able to store potassium ions with low lattice strain and slight volume change,^[37–39] therefore being an ideal anode for stable and high-voltage KIMSCs. Nevertheless, the rational design of KIMSCs remains unexplored so far.

Herein, we reported a new prototype of high-performance KIMSCs based on MXene-derived KTO nanorods as negative electrode and porous activated graphene (AG) as positive electrode in a non-flammable high-voltage ionogel electrolyte, which served as a sufficient microscale power source for the construction of an integrated sensor system. The KTO nanorods were prepared from the simultaneous alkalization and oxidation of Ti₃C₂ MXene via hydrothermal method. Impressively, the KTO delivered a considerable diffusion coefficient of $1.6 \times 10^{-12} \text{ cm}^2 \text{ s}^{-1}$ and high capacity of 145 mAh g^{-1} as anode materials for K ion storage. The as-fabricated KIMSCs could offer a large operating voltage of 3.8 V, extraordinary volumetric

energy density of 34.1 mWh cm^{-3} , and mechanical robustness. Besides, a highly integrated system based on our KIMSC and a pressure sensor was well designed for efficiently monitoring the body movement of elbow and finger.

2. Results and Discussion

The preparation process of MXene (Ti₃C₂)-derived potassium titanate (K₂Ti₈O₁₇, KTO) nanorods was schematically illustrated in **Figure 1a**. Briefly, the accordion-like Ti₃C₂ MXene was initially synthesized by selectively etching the Al interlayer of pristine Ti₃AlC₂ in the etchant of hydrofluoric acid solution (Figure S1, Supporting Information).^[40,41] Next, Ti₃C₂ MXene was subjected to hydrothermal treatment for simultaneous oxidation and alkalization in H₂O₂ and KOH solution at 180 °C. To optimize the morphology, KTO synthesized at different KOH concentration ($x \text{ mol L}^{-1}$) and treatment time ($y \text{ h}$) (denoted as KTO- x - y) was discussed. As shown in Figure 1b,c, KTO-10-24 exhibited a uniform and elongated nanorod structure with a length of 1–5 μm and width of 100–200 nm. The typical diffraction peaks at 11.1°, 24.1°, 28.8°, and 48.0° (Figure S2, Supporting Information) were well indexed to the standard PDF card (JCPDS No 41-1100), corresponding to the chemical formula of K₂Ti₈O₁₇. However, when KOH concentration decreased, KTO-1-24 and KTO-5-24 showed an irregular small particle and interlaced filament (Figure S3, Supporting Information), respectively. When the treatment time was prolonged, KTO-10-48 nanorods became

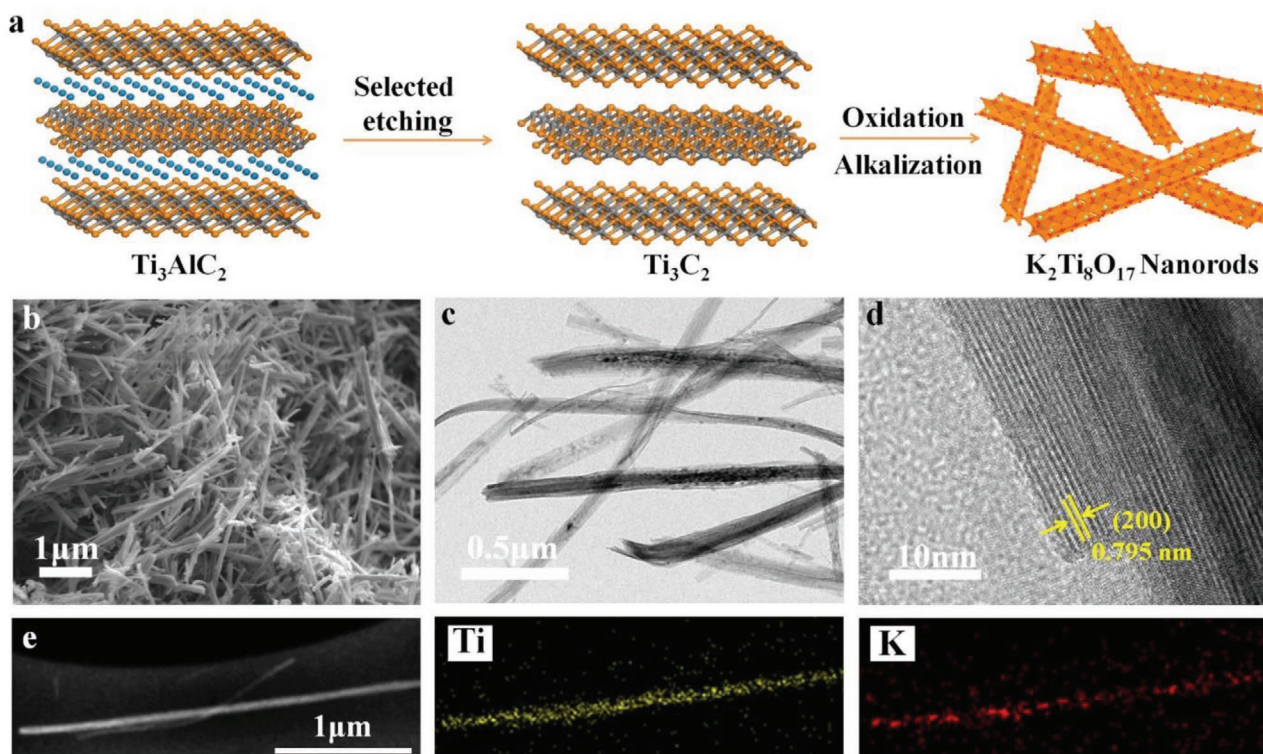


Figure 1. The preparation and morphology of MXene-derived KTO nanorods. a) Schematic illustration of the preparation process of KTO nanorods from simultaneous oxidation and alkalization of Ti₃C₂ MXene in 10 m KOH at 180 °C for 24 h. b–e) SEM image (b), TEM image (c), HRTEM image (d) and elemental mapping analysis (e) of KTO nanorods.

bolder due to the prolonged hydrothermal time. Thus, the optimal condition of hydrothermal treatment for KTO nanorods preparation was 10 M KOH for 24 h. High-resolution transmission electron microscopy (HRTEM) images revealed a crystal-line structure of KTO-10-24 nanorods with a large interlayer spacing of 0.795 nm (Figure 1d), in agreement with the (200) plane of X-ray diffraction (XRD) pattern. X-ray photoelectron spectroscopy (XPS) spectrum confirmed the distinguishable signals of K 2p and Ti 2p in KTO-10-24 nanorods (Figure S4, Supporting Information). Also, potassium and titanium elements were well discerned in KTO-10-24 nanorods (Figure 1e), highlighting the homogenous distribution of Ti and K.

The electrochemical performance of KTO was then evaluated for potassium ion storage in 0.8 M KPF₆ electrolyte at a potential range of 0.01–3 V (vs K⁺/K) (Figure 2). Apart from the irreversibly broad discharge peak below 1.5 V in the first

discharge cycle, the subsequent cycles were almost overlapped (Figure S5, Supporting Information), suggesting completely reversible process. Furthermore, the reversible peaks below 0.5 V in the 2nd and 3rd cycles were assigned to the valence change from Ti⁴⁺ to Ti³⁺. As a result, KTO-10-24 nanorods delivered a reversible capacity of 145 mAh g⁻¹ at 20 mA g⁻¹ (Figure 2a,b). This capacity value was higher than KTO-1-24 (124.7 mAh g⁻¹), KTO-5-24 (120 mAh g⁻¹), KTO-10-48 (105.6 mAh g⁻¹) and other reported KTO (Table S1, Supporting Information), such as K₂Ti₆O₁₃ (95 mAh g⁻¹ at 20 mA g⁻¹),^[42] and K₂Ti₄O₉ (97 mAh g⁻¹ at 30 mA g⁻¹).^[38] With increasing current densities from 50, 100, 150, 200 to 300 mA g⁻¹, KTO-10-24 delivered a highly reversible capacities of 106, 97, 90, 84 to 76 mAh g⁻¹, respectively, indicative of extraordinary rate performance. Additionally, the electrochemical impedance spectroscopy (EIS, Figure 2c) showed that the Nyquist plots of all KTO

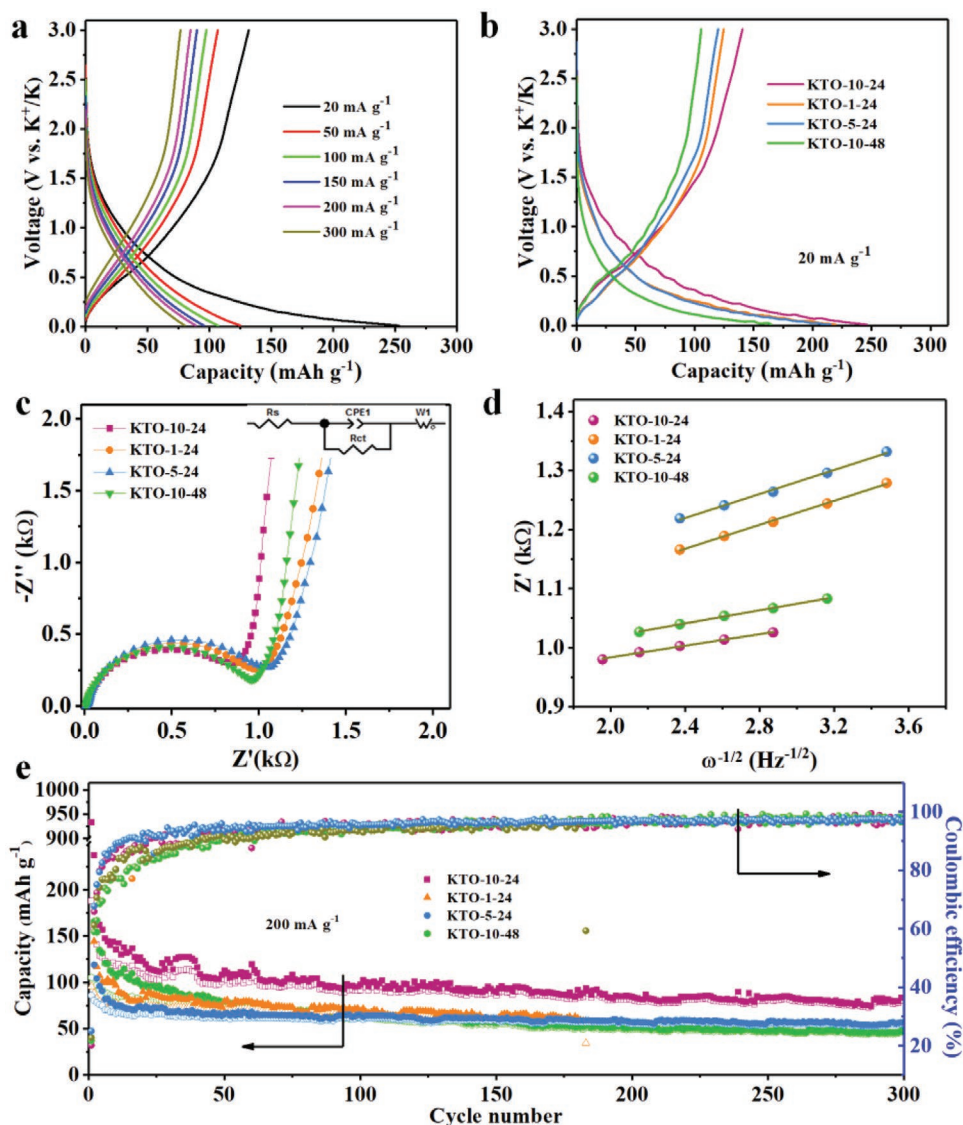


Figure 2. Electrochemical characterization of KTO nanorods for potassium ion storage. a) GCD profiles of KTO-10-24 measured from 20 to 300 mA g⁻¹. b–e) GCD profiles (b) at 20 mA g⁻¹, EIS spectra (c), linear fitting of Z' versus $\omega^{-1/2}$ in the low-frequency region (d), and long-term cycling performance (e) of various KTO samples. Inset of (c) is the equivalent circuit.

materials consisted of a semicircle shape in high frequency and steep line in low frequency (Warburg region), corresponding to the charge transfer resistance (R_{ct}) and K cation diffusion coefficient (D_K^+) in KTO. Specifically, KTO-10-24 disclosed a small R_{ct} of 589 Ω (Table S2, Supporting Information), lower than KTO-1-24 (762 Ω), KTO-5-24 (796 Ω), and KTO-10-48 (802 Ω), revealing a favorable interfacial charge transport. Moreover, the plots of Z' versus $\omega^{-1/2}$ reflected the Warburg factor (σ , Figure 2d) and then was used to evaluate the D_K^+ (Table S1, Supporting Information). Accordingly, the D_K^+ of KTO-10-24 was calculated to be 1.6×10^{-12} $\text{cm}^2 \text{s}^{-1}$, which was obviously higher than KTO-1-24 (3.4×10^{-13} $\text{cm}^2 \text{s}^{-1}$), KTO-5-24 (3.3×10^{-13} $\text{cm}^2 \text{s}^{-1}$), and KTO-10-48 (1.1×10^{-12} $\text{cm}^2 \text{s}^{-1}$). These results implied that KTO-10-24 with large interlayer spacing and high length-diameter ratio could greatly promote the transfer of ions and electrons, therefore benefiting a better electrochemical performance. Remarkably, KTO-10-24 exhibited considerable long-term cyclability for continuous 300 cycles at 200 mA g^{-1} (Figure 2e), and the negligible capacity delay was achieved after 200 cycles, indicative of the promising candidate in K ion storage.

To further demonstrate the feasibility of flexible electronics, KIMSCs consisting of KTO nanorods anode and AG cathode were assembled on a flexible nylon membrane via a customized mask-assisted deposition method (Figure 3a, see details in Supporting Information).^[43,44] The porous AG was obtained from reduced graphene oxide aerogels with KOH activation,^[45] having a high specific surface area of ≈ 2300 $\text{m}^2 \text{g}^{-1}$ with a pore size distribution of 2.5 nm (Figure S6, Supporting Information). The electrochemically exfoliated graphene (EG) nanosheets were employed as metal-free current collectors, highly conductive additives, and strongly flexible support (≈ 1000 S cm^{-1} , Figure S7, Supporting Information). Typically, the as-prepared microelectrodes of KTO and AG had a thickness of ≈ 5 μm and ≈ 14 μm (Figure S8, Supporting Information), respectively. It could be observed that the EG nanosheets were interlaced into adjacent active materials of KTO and AG, resulting in the formation of conducting channels for both microelectrodes. Furthermore, scanning electron microscopy (SEM) images indicated that the overlapping of KTO/EG or AG/EG enabled efficient construction of a highly conductive network in each electrode for fast electron transfer (Figure S9, Supporting Information). As a consequence, the electrical conductivities reached to ≈ 350 S cm^{-1} for KTO anode and ≈ 100 S cm^{-1} for AG cathode (Figure S10, Supporting Information). Meanwhile, we also verified the excellent flexibility by bending, rolling, and twisting the paper-like KIMSCs (Figure S11, Supporting Information), remaining the integrity without any damage.

To implement high-safety KIMSCs for flexible electronics, we also prepared a nonflammable ionogel electrolyte, made up of bis(trifluoromethylsulfonyl) imide potassium salt (KTFSI), 1-butyl-1-methylpyrrolidinium bis(trifluoromethylsulfonyl) imide (P_{14}TFSI), and poly(vinylidene difluoride-co-hexafluoropropylene) (PVDF-HFP) (denoted as KTFSI-IE). Remarkably, different from the conventional organic gel electrolyte, KPF_6 in ethylene carbonate and dimethyl carbonate mixed with PVDF-HFP, the as-prepared KTFSI-IE was thermo-stable up to ≈ 370 $^\circ\text{C}$ (Figure S12, Supporting Information), and was flame resistant in air even after 15 s (Figure S13, Supporting Information). The

electrochemical stability of KTFSI-IE was also certified through linear sweep voltammetry (LSV, Figure 3c). An anodic oxidation occurred from LSV curve when the potential increased to 4.8 V, suggestive of wide stability voltage of KTFSI-IE. Notably, the stable KTFSI-IE delivered a decent ionic conductivity of 1.3 mS cm^{-1} at room temperature (Figure 3b). Moreover, the ionic conductivity of KTFSI-IE increased with the temperature, in which the ionic conductivity reached up to 6.8 mS cm^{-1} at 100 $^\circ\text{C}$. Such robust stability and intrinsic electrochemical character of KTFSI-IE would enable high performance for KIMSCs. The flexible solid-state KIMSCs were then assembled through drop-casting KTFSI-IE onto the surface of microelectrodes, followed by solidification process (Figure 3a).

To validate the excellent electrochemical performance, galvanometric charge and discharge (GCD) test was carried out at a voltage window of 0–3.8 V (Figure 3d). According to the discharge profiles, the gradual lines between 1.5 and 3.5 V were attributed to the successful match between intercalation-type KTO anode and non-Faradaic AG cathode. Based on the optimal thickness ratio of 1:3 for anode to cathode (Figure S14, Supporting Information), the KIMSCs presented high areal and volumetric capacitance of 12.8 mF cm^{-2} and 13.5 F cm^{-3} at 30 $\mu\text{A cm}^{-2}$, respectively (Figure 3e), much higher than the reported graphene (G)// $\text{K}_2\text{Co}_3(\text{P}_2\text{O}_7)_2 \cdot 2\text{H}_2\text{O}$ MSCs (6.0 F cm^{-3}).^[46] At high current density of 200 $\mu\text{A cm}^{-2}$, a considerable areal and volumetric capacitance of 7.7 mF cm^{-2} and 8.2 F cm^{-3} remained, respectively, suggestive of robust rate performance. The conductive EG additives in KIMSCs made a low equivalent serial resistance (334 Ω , Figure S15, Supporting Information), but contributed a fairly tiny part ($\approx 2.4\%$) to the entire capacitance of KIMSCs (Figure S16, Supporting Information). Notably, the voltage of KIMSCs was as high as 3.8 V. To the best of our knowledge, this value is the highest among the reported MSCs, for instance, MnO_2 -polyppyrrrole (PPy)// V_2O_5 -polyaniline (PANI) (1.6 V),^[47] laser-induced graphene (LIG)- FeOOH //LIG- MnO_2 (1.8 V),^[48] EG-MXene//EG-MXene (3.0 V),^[49] F-doped graphene (FG)//FG (3.5 V),^[50] and EG-VS₂//activated carbon (3.5 V).^[51] Furthermore, our KIMSCs delivered a high volumetric energy density of 34.1 mWh cm^{-3} at a power density of 75 mW cm^{-3} , superior to the most reported works (Figure 3f), such as MnO_2 -PPy// V_2O_5 -PANI (19.8 mWh cm^{-3}),^[47] EG// MnO_2 -PH1000 (6.6 mWh cm^{-3}),^[52] LIG- FeOOH //LIG- MnO_2 (2.4 mWh cm^{-3})^[48] and G// $\text{K}_2\text{Co}_3(\text{P}_2\text{O}_7)_2 \cdot 2\text{H}_2\text{O}$ (0.96 mWh cm^{-3}).^[46] The KIMSCs showed a maximum power density of 828 mW cm^{-3} , corresponding to a high energy density of 14.3 mWh cm^{-3} (Figure S17, Supporting Information). In addition, the mechanically robust feature could be verified by nearly unchanged GCD profiles (Figure 3g) and overlapped cyclic voltammetry (CV) curves (Figure S18, Supporting Information) with varying bending angles from flat to 180 $^\circ$. Moreover, the long-term stability of flexible KIMSCs could be demonstrated by 82% retention of the initial capacitance and unchanged Coulombic efficiency over 5000 cycles (Figure 3h). Overall, we ascribed the prominent performances of our KIMSCs to the factors including combined strategies of outstanding conductive network in microelectrodes, highly electrochemical activity of KTO and AG, distinguished ionic conductivity of KTFSI-IE, and strong interfacial coupling between electrodes and flexible substrate.

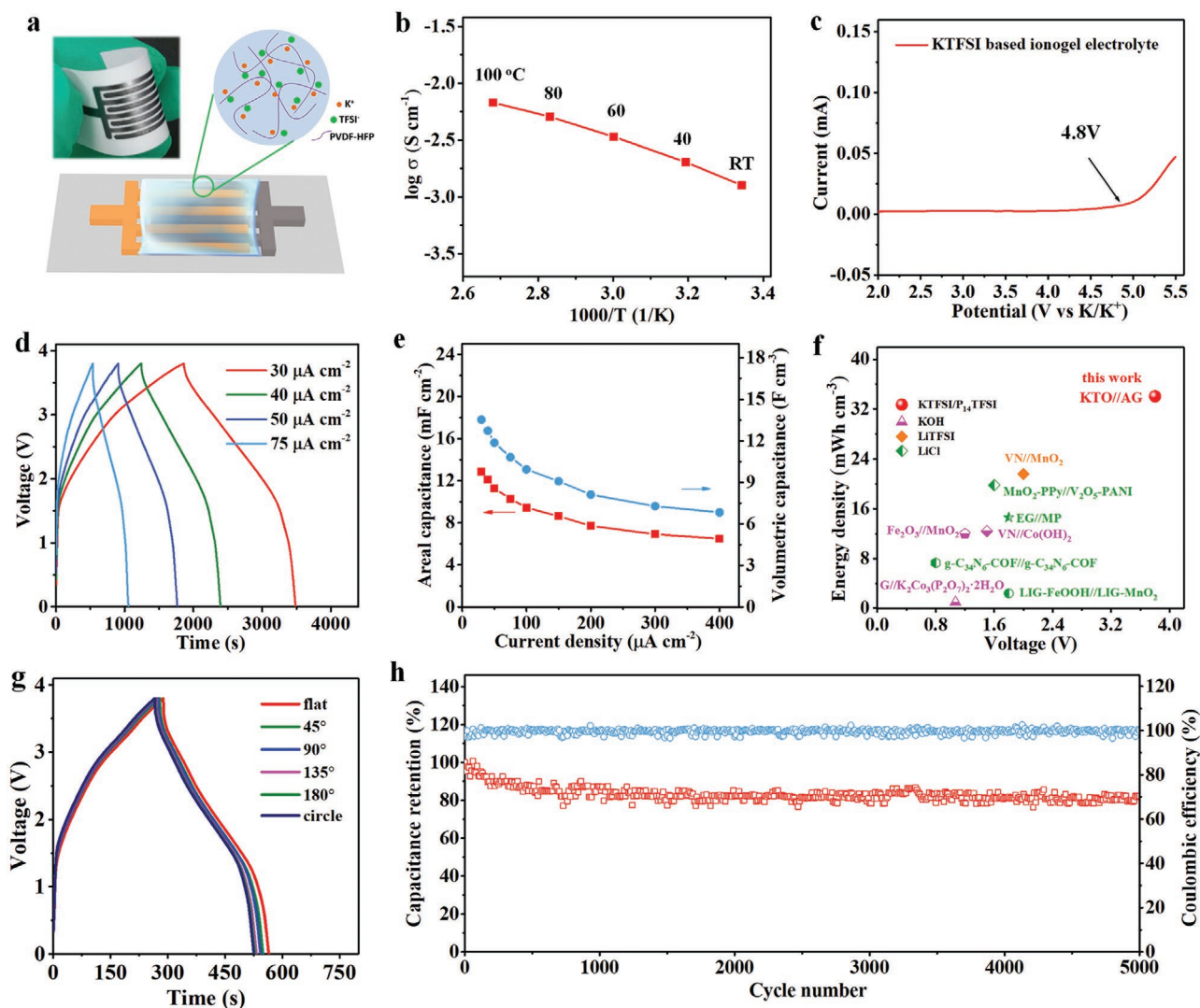


Figure 3. Characterization of iongel electrolyte and electrochemical performance of KIMSCs. a) Schematic diagram and optical image of KIMSCs with KTFSE-IE. b) Ionic conductivities of KTFSE-IE at different temperature. c) LSV curve of KTFSE-IE at 2 mV s^{-1} . d) GCD profiles of KIMSCs recorded from 30 to $75 \mu\text{A cm}^{-2}$. e) Areal capacitance and volumetric capacitance of KIMSCs obtained from 30 to $400 \mu\text{A cm}^{-2}$. f) Volumetric energy density versus voltage of KIMSCs in comparison to previous works. g) GCD profiles tested at various bending angle from flat to 180° . h) Long-term cycling performance of KIMSCs for 5000 cycles obtained at 0.3 mA cm^{-2} .

To understand the ions storage process, the kinetic analysis of KIMSCs was further performed via CV measurement. The CV curves tested from 1 to 5 mV s^{-1} showed a proportionally increased current along with the scan rates (Figure 4a). Generally, the current could be separated to diffusion-controlled contribution and pseudocapacitive contribution, following the equation: $i = av^b$, where i is the current from CV curves, v is the scan rate, a and b are the constant terms. $b = 0.5$ means the diffusion-controlled process, and $b = 1$ indicates the surface-controlled pseudocapacitive process. According to the power-law relationship, b value was evaluated to be 0.85 and 0.87 for the anodic peak and cathodic peak (Figure 4b), respectively. It implied a mixed behavior of diffusion-controlled contribution and pseudocapacitive contribution for KIMSCs. Furthermore, the contribution ratio of the surface-controlled (k_1v) and diffusion-controlled ($k_2v^{0.5}$) effects

could be quantitatively separated by the following formula: $i = k_1v + k_2v^{0.5}$, where k_1 and k_2 , the variable constant, characterize the surface-controlled and diffusion-controlled behaviors at a fixed scan rate and voltage, respectively. From the quantitative analysis, the surface-controlled contribution increased with the scan rate and a larger than 67% of the entire capacitance was driven from the surface-controlled effect (Figure 4c; Figure S19, Supporting Information), demonstrating a dominating capacitive contribution of KIMSCs with a fast kinetics.

Furthermore, the ions storage behavior of KIMSCs during charge and discharge process were studied by in situ Raman and ex situ XRD analyses in a full device. As shown in Figure 4d,e, KIMSCs with planar interdigital pattern can be directly probed via Raman beam, unlike punching metal current collector of the conventionally stacked energy storage devices. Before charging, the peaks of KTO anode located at

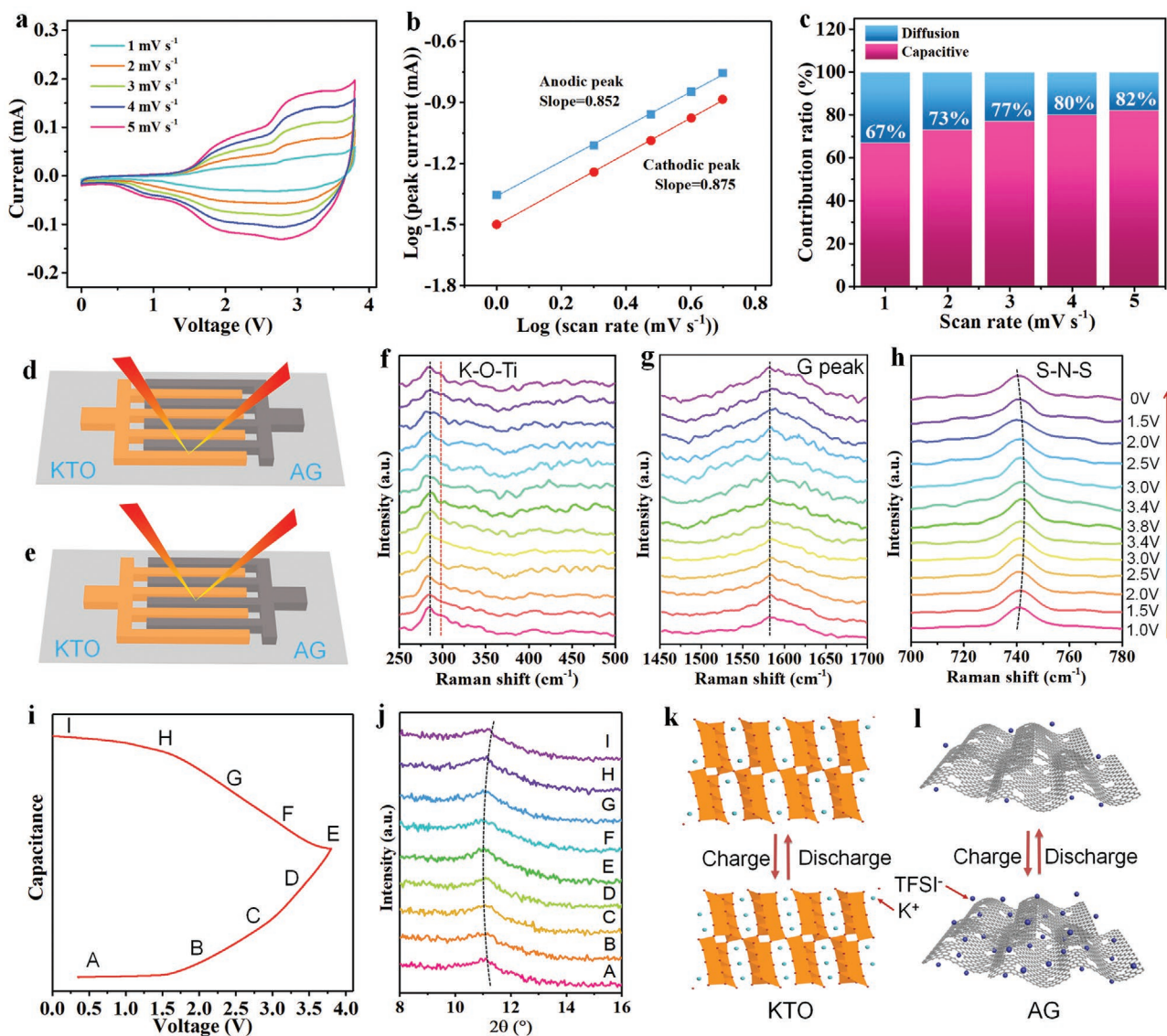


Figure 4. Kinetic analysis and in (ex) situ studies of KIMSCs. a) CV curves measured from 1 to 5 mV s^{-1} . b) Anodic and cathodic current response as a function of scan rate. c) The normalized pseudocapacitive and diffusion-controlled contribution at different scan rates. d, e) Schematic illustration of in situ Raman spectra of KIMSCs for KTO anode (d) and AG cathode (e). f–h) Raman spectra of KTO (f), AG (g), and TFSI anion (h) obtained from AG cathode. i) GCD profile showing the positions for ex situ XRD patterns. j) The ex situ XRD patterns of KTO anode. k, l) Schematic diagram displaying structural models of KTO anode (k) and AG cathode (l) at the starting charge (top) and discharge (bottom) process.

282 and 295 cm^{-1} were assigned to the K–O–Ti stretching vibration (Figure 4f). The peak at 1585 cm^{-1} originated from the in-plane vibration (G peak) of AG cathode (Figure 4g). The peak at 741 cm^{-1} stemmed from the bending vibration of S–N–S bond in TFSI anion (Figure 4h), which was obtained from AG cathode. During charging, the intensity of the peak at 295 cm^{-1} gradually decreased and disappeared (Figure 4f), implying the possible intercalation of K cation into the bulk KTO. The position of G peak remained unchanged (Figure 4g), indicative of the intact structure of AG without ion intercalation. Meanwhile, the vibration of S–N–S bond from TFSI anion drifted from 741 to 743 cm^{-1} (Figure 4h), suggesting the adsorption-enrichment effect of TFSI anion in the interface of AG cathode during the charge process. Besides, ex situ XRD measurement was applied

to investigate the structural evolution of KTO in KIMSCs (Figure 4i,j). During potassiation process, the (200) plane diffraction peak at 11.1° gradually shifted to a low angle of 10.9°, due to the insertion of K cation. Correspondingly, the interlayer spacing of (200) plane was slightly expanded from 0.795 to 0.807 nm. After discharge process, all of the vibration peaks at Raman spectra and diffraction peaks at XRD patterns recovered to the original positions, suggestive of highly reversible deintercalation of K cation and desorption of TFSI anion. In terms of the aforementioned analysis, it is concluded that the K cation insertion/extraction process on KTO and TFSI anion adsorption/desorption process on AG are synchronous with tiny volume change during charge and discharge processes (Figure 4k,l).

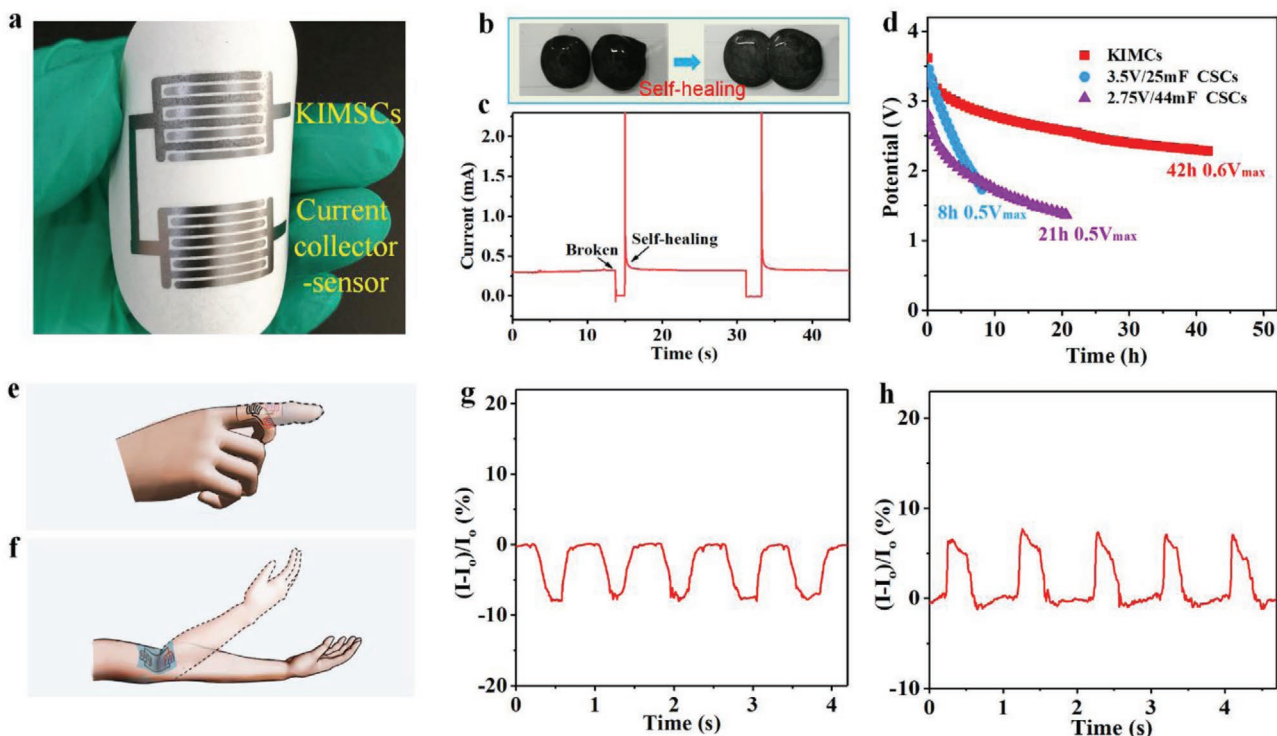


Figure 5. Performance of the integrated KIMSC-sensor system. a) Photograph of the integrated KIMSC-sensor system. b,c) Photograph (b) and current response (c) of the pressure-sensing graphene-based PVA hydrogel to show the self-healing process. d) Self-discharge process of KIMSCs from V_{\max} to $0.6 V_{\max}$. e,f) Schematic images to show the attached KIMSC-sensor system on the finger and elbow. g,h) Current change of graphene-based hydrogel sensor powered by a KIMSC in response to finger bending (g) and elbow bending (h).

To demonstrate the potential of KIMSCs in smart devices, a flexible integrated system consisted of a planar KIMSC and graphene-based pressure sensor was constructed through the simple mask-assisted filtration strategy (Figure 5a; Figures S20 and S21, Supporting Information). In such a system, the highly conductive EG nanosheets served as the metal-free interconnection and interdigital current collector for a KIMSC and sensor, enabling a fully flexible function integration. To realize the pressure sensor, conductive graphene-based hydrogel as pressure sensing material was prepared from graphene and polyvinyl alcohol (PVA) dispersion uniformly mixed with cross-linked agent of borax, where tetrafunctional borate ion has an interaction with $-\text{OH}$ group in PVA via hydrogen-bonding. Graphene filler in the pressure sensitive hydrogel with a suitable concentration (≈ 1 wt%) could form an efficiently electrically conductive network in a nanoscale to dramatically improve the piezoresistivity.^[53–57] As shown in Figure 5b, the conductive graphene-based hydrogel was able to be fast self-healed without any external stimuli after being totally separated, due to the reformation of hydrogen-bonding interaction.^[58,59] Such a robust self-healing process was also proved by the current change over time (Figure 5c). When the graphene-based hydrogel was completely severed, the current immediately decreased to zero owing to the open circuit. Once the spontaneous healing occurred, the current fleetly recovered to the initial value with a self-healing efficiency of $\approx 99\%$. The rapid self-healing process of graphene-based hydrogel rendered a repeatable restoration of electrical response, therefore

satisfying piezoresistive pressure sensor. In addition, the KIMSC showed a long self-discharge time from 3.8 V (V_{\max}) to 2.4 V ($0.6 V_{\max}$) over 44 h (Figure 5d), much higher than the 3.5 V per 25 mF commercial supercapacitors (CSCs, 8 h) and 2.75 V per 44 mF CSCs (21 h) at $0.5 V_{\max}$.^[60] As an integrated sensor system, the KIMSC could provide the efficient power for body motion detection (e.g., finger joint, elbow) and bending monitor via an electromechanical response (Figure 5e,f and Video S1, Supporting Information). For instance, when the integrated system was attached onto the finger joint to detect the repeated bending motion, a stable response with $\approx 8\%$ variation of the original current was detected (Figure 5g), attributed to the tensile behavior of graphene-based hydrogel. When attached on the elbow under movement, the integrated system disclosed a positive current response with $\approx 7\%$ variation (Figure 5h), due to the compressive effect of the deformation. Therefore, it is verified that our KIMSCs as a standalone power source could well power the wearable pressure sensor in an integrated system to register the body motion with a clear response, paving a way for wearable microelectronics.

3. Conclusion

In summary, we have developed MXene-derived KTO nanorods based KIMSCs as an integrated electronic unit for micro-scale energy storage and utilization. The KTO nanorods from the simultaneous alkalization and oxidation of Ti_3C_2 MXene

delivered a large ion diffusion coefficient and higher capacity of 145 mAh g⁻¹. Planar KIMSCs with interdigital pattern of KTO nanorods anode and AG cathode delivered a high voltage of 3.8 V, an extraordinary volumetric energy density of 34.1 mWh cm⁻³ and outstanding flexibility. Moreover, the highly integrated pressure sensing system of a KIMSC and sensor could sensitively record motion detection. Through the reasonable design and good match of anode and cathode, exploitation of stable and high-voltage electrolyte and development of the compatible technologies, it is believed that KIMSCs will further present notable electrochemical performance and become a highly-competitive microscale power source for microelectronics.

Supporting Information

Supporting Information is available from the Wiley Online Library or from the author.

Acknowledgements

S.Z. and J.M. contributed equally to this work. This work was financially supported by the National Key R&D Program of China (Grants 2016YBF0100100, 2016YFA0200200), the National Natural Science Foundation of China (Grant Nos. 51872283, 22075279, 21805273, 22005297, 22005298), Dalian National Laboratory For Clean Energy (DNL), CAS, DNL Cooperation Fund, CAS (DNL180310, DNL180308, DNL201912, and DNL201915), the Liao Ning Revitalization Talents Program (Grant XLYC1807153), the Natural Science Foundation of Liaoning Province, Joint Research Fund Liaoning-Shenyang National Laboratory for Materials Science (Grant 20180510038), the central government of Liaoning Province guides the funds for local science and technology development (Grant 2021JH6/10500112), Dalian Innovation Support Plan for High Level Talents (2019RT09), DICP (DICP ZZBS201708, DICP ZZBS201802, DICP I2020032), DICP&QIBEBT (Grant DICP&QIBEBT UN201702), and China Postdoctoral Science Foundation (2019M661141).

Conflict of Interest

The authors declare no conflict of interest.

Data Availability Statement

Research data are not shared.

Keywords

integrated systems, ionogel electrolytes, MXenes, potassium ion micro-supercapacitors, potassium titanate

Received: December 10, 2020

Revised: February 15, 2021

Published online: March 18, 2021

[1] S. Park, S. W. Heo, W. Lee, D. Inoue, Z. Jiang, K. Yu, H. Jinno, D. Hashizume, M. Sekino, T. Yokota, K. Fukuda, K. Tajima, T. Someya, *Nature* **2018**, 561, 516.

- [2] D. Son, J. Kang, O. Vardoulis, Y. Kim, N. Matsuhisa, J. Y. Oh, J. W. F. To, J. Mun, T. Katsumata, Y. Liu, A. F. McGuire, M. Krason, F. Molina-Lopez, J. Ham, U. Kraft, Y. Lee, Y. Yun, J. B. H. Tok, Z. Bao, *Nat. Nanotechnol.* **2018**, 13, 1057.
- [3] C.-M. Horejs, *Nat. Rev. Mater.* **2018**, 3, 18002.
- [4] D. H. Kim, N. S. Lu, R. Ma, Y. S. Kim, R. H. Kim, S. D. Wang, J. Wu, S. M. Won, H. Tao, A. Islam, K. J. Yu, T. I. Kim, R. Chowdhury, M. Ying, L. Z. Xu, M. Li, H. J. Chung, H. Keum, M. McCormick, P. Liu, Y. W. Zhang, F. G. Omenetto, Y. G. Huang, T. Coleman, J. A. Rogers, *Science* **2011**, 333, 838.
- [5] P. Huang, C. Lethien, S. Pinaud, K. Brousse, R. Laloo, V. Turq, M. Respaud, A. Demortière, B. Daffos, P. L. Taberna, B. Chaudret, Y. Gogotsi, P. Simon, *Science* **2016**, 351, 691.
- [6] K.-H. Lee, S.-S. Lee, D. B. Ahn, J. Lee, D. Byun, S.-Y. Lee, *Sci. Adv.* **2020**, 6, eaaz1692.
- [7] P. Zhang, F. Wang, M. Yu, X. Zhuang, X. Feng, *Chem. Soc. Rev.* **2018**, 47, 7426.
- [8] H. L. Ning, J. H. Pikul, R. Y. Zhang, X. J. Li, S. Xu, J. J. Wang, J. A. Rogers, W. P. King, P. V. Braun, *Pro. Natl. Acad. Sci. U. S. A.* **2015**, 112, 6573.
- [9] Z. S. Wu, K. Parvez, X. L. Feng, K. Müllen, *Nat. Commun.* **2013**, 4, 2487.
- [10] Z.-S. Wu, Y.-Z. Tan, S. Zheng, S. Wang, K. Parvez, J. Qin, X. Shi, C. Sun, X. Bao, X. Feng, K. Müllen, *J. Am. Chem. Soc.* **2017**, 139, 4506.
- [11] S. Zheng, X. Shi, P. Das, Z.-S. Wu, X. Bao, *Adv. Mater.* **2019**, 31, 1900583.
- [12] D. Pech, M. Brunet, H. Durou, P. H. Huang, V. Mochalin, Y. Gogotsi, P. L. Taberna, P. Simon, *Nat. Nanotechnol.* **2010**, 5, 651.
- [13] D. Qi, Y. Liu, Z. Liu, L. Zhang, X. Chen, *Adv. Mater.* **2017**, 29, 1602802.
- [14] S. Zheng, J. Ma, Z.-S. Wu, F. Zhou, Y. He, F. Kang, H.-M. Cheng, X. Bao, *Energy Environ. Sci.* **2018**, 11, 2001.
- [15] Y. Shao, M. F. El-Kady, J. Sun, Y. Li, Q. Zhang, M. Zhu, H. Wang, B. Dunn, R. B. Kaner, *Chem. Rev.* **2018**, 118, 9233.
- [16] S. Zheng, Z.-S. Wu, S. Wang, H. Xiao, F. Zhou, C. Sun, X. Bao, H.-M. Cheng, *Energy Storage Mater.* **2017**, 6, 70.
- [17] J. Ding, W. Hu, E. Paek, D. Mitlin, *Chem. Rev.* **2018**, 118, 6457.
- [18] J. L. Liu, J. Wang, C. H. Xu, H. Jiang, C. Z. Li, L. L. Zhang, J. Y. Lin, Z. X. Shen, *Adv. Sci.* **2018**, 5, 1700322.
- [19] M. R. Lukatskaya, B. Dunn, Y. Gogotsi, *Nat. Commun.* **2016**, 7, 12647.
- [20] X. Y. Shan, Y. Z. Wang, D. W. Wang, F. Li, H. M. Cheng, *Adv. Energy Mater.* **2016**, 6, 1502064.
- [21] Y. Liu, Y. J. Fang, Z. W. Zhao, C. Z. Yuan, X. W. Lou, *Adv. Energy Mater.* **2019**, 9, 1803052.
- [22] B. J. Yang, J. T. Chen, S. L. Lei, R. S. Guo, H. X. Li, S. Q. Shi, X. B. Yan, *Adv. Energy Mater.* **2018**, 8, 1702409.
- [23] N. Yabuuchi, K. Kubota, M. Dahbi, S. Komaba, *Chem. Rev.* **2014**, 114, 11636.
- [24] H. Kim, J. C. Kim, M. Bianchini, D. H. Seo, J. Rodriguez-Garcia, G. Ceder, *Adv. Energy Mater.* **2018**, 8, 1702384.
- [25] R. Zhao, H. Di, X. Hui, D. Zhao, R. Wang, C. Wang, L. Yin, *Energy Environ. Sci.* **2020**, 13, 246.
- [26] Z. Xiao, J. Meng, F. Xia, J. Wu, F. Liu, X. Zhang, L. Xu, X. Lin, L. Mai, *Energy Environ. Sci.* **2020**, 13, 3129.
- [27] H. W. Huang, J. Cui, G. X. Liu, R. Bi, L. Zhang, *ACS Nano* **2019**, 13, 3448.
- [28] J. Y. Zhang, P. X. Cui, Y. Gu, D. J. Wu, S. Tao, B. Qian, W. S. Chu, L. Song, *Adv. Mater. Interfaces* **2019**, 6, 1901066.
- [29] W. C. Zhang, Y. J. Liu, Z. P. Guo, *Sci. Adv.* **2019**, 5, eaav7412.
- [30] Y. Wu, H. B. Huang, Y. Z. Feng, Z. S. Wu, Y. Yu, *Adv. Mater.* **2019**, 31, 1901414.
- [31] H. T. Tan, Y. Z. Feng, X. H. Rui, Y. Yu, S. M. Huang, *Small Methods* **2020**, 4, 1900563.

- [32] K. M. Song, C. T. Liu, L. W. Mi, S. L. Chou, W. H. Chen, C. Y. Shen, *Small* **2019**, *17*, 1903194.
- [33] M. Z. Ma, S. P. Zhang, Y. Yao, H. Y. Wang, H. J. Huang, R. Xu, J. W. Wang, X. F. Zhou, W. J. Yang, Z. Q. Peng, X. J. Wu, Y. L. Hou, Y. Yu, *Adv. Mater.* **2020**, *32*, 2000958.
- [34] Z. Zhang, M. Li, Y. Gao, Z. Wei, M. Zhang, C. Wang, Y. Zeng, B. Zou, G. Chen, F. Du, *Adv. Funct. Mater.* **2018**, *28*, 1802684.
- [35] D. M. Xu, D. L. Chao, H. W. Wang, Y. S. Gong, R. Wang, B. B. He, X. L. Hu, H. J. Fan, *Adv. Energy Mater.* **2018**, *8*, 1702769.
- [36] H. L. Qiu, L. Zhao, M. Asif, X. X. Huang, T. Y. Tang, W. Li, T. Zhang, T. Shen, Y. L. Hou, *Energy Environ. Sci.* **2020**, *13*, 571.
- [37] N. Wang, C. Chu, X. Xu, Y. Du, J. Yang, Z. Bai, S. Dou, *Adv. Energy Mater.* **2018**, *8*, 1801888.
- [38] B. Kishore, G. Venkatesh, N. Munichandraiah, *J. Electroanal. Chem.* **2016**, *163*, A2551.
- [39] K. Z. Cao, H. Q. Liu, W. Y. Li, C. X. Xu, Q. Q. Han, Z. Zhang, L. F. Jiao, *J. Electroanal. Chem.* **2019**, *841*, 51.
- [40] M. Naguib, M. Kurtoglu, V. Presser, J. Lu, J. Niu, M. Heon, L. Hultman, Y. Gogotsi, M. W. Barsoum, *Adv. Mater.* **2011**, *23*, 4248.
- [41] M. R. Lukatskaya, O. Mashtalir, C. E. Ren, Y. Dall'Agnese, P. Rozier, P. L. Taberna, M. Naguib, P. Simon, M. W. Barsoum, Y. Gogotsi, *Science* **2013**, *341*, 1502.
- [42] S. Dong, Z. Li, Z. Xing, X. Wu, X. Ji, X. Zhang, *ACS Appl. Mater. Interfaces* **2018**, *10*, 15542.
- [43] H. Xiao, Z.-S. Wu, L. Chen, F. Zhou, S. Zheng, W. Ren, H.-M. Cheng, X. Bao, *ACS Nano* **2017**, *11*, 7284.
- [44] S. Zheng, H. Huang, Y. Dong, S. Wang, F. Zhou, J. Qin, C. Sun, Y. Yu, Z.-S. Wu, X. Bao, *Energy Environ. Sci.* **2020**, *13*, 821.
- [45] Y. Zhu, S. Murali, M. D. Stoller, K. J. Ganesh, W. Cai, P. J. Ferreira, A. Pirkle, R. M. Wallace, K. A. Cyhosh, M. Thommes, D. Su, E. A. Stach, R. S. Ruoff, *Science* **2011**, *332*, 1537.
- [46] H. Pang, Y. Zhang, W.-Y. Lai, Z. Hu, W. Huang, *Nano Energy* **2015**, *15*, 303.
- [47] Y. Yue, Z. Yang, N. Liu, W. Liu, H. Zhang, Y. Ma, C. Yang, J. Su, L. Li, F. Long, Z. Zou, Y. Gao, *ACS Nano* **2016**, *10*, 11249.
- [48] Y. Huang, X. Bai, M. Zhou, S. Liao, Z. Yu, Y. Wang, H. Wu, *Nano Lett.* **2016**, *16*, 5846.
- [49] S. Zheng, C. Zhang, F. Zhou, Y. Dong, X. Shi, V. Nicolosi, Z.-S. Wu, X. Bao, *J. Mater. Chem. A* **2019**, *7*, 9478.
- [50] F. Zhou, H. Huang, C. Xiao, S. Zheng, X. Shi, J. Qin, Q. Fu, X. Bao, X. Feng, K. Müllen, Z.-S. Wu, *J. Am. Chem. Soc.* **2018**, *140*, 8198.
- [51] P. Zhang, L. Wang, F. Wang, D. Tan, G. Wang, S. Yang, M. Yu, J. Zhang, X. Feng, *Batteries Supercaps* **2019**, *2*, 918.
- [52] X. Shi, Z.-S. Wu, J. Qin, S. Zheng, S. Wang, F. Zhou, C. Sun, X. Bao, *Adv. Mater.* **2017**, *29*, 1703034.
- [53] O. Zetina-Hernández, S. Duarte-Aranda, A. May-Pat, G. Canché-Escamilla, J. Uribe-Calderon, P. I. Gonzalez-Chi, F. Avilés, *J. Mater. Sci.* **2013**, *48*, 7587.
- [54] Y. Ema, M. Ikeya, M. Okamoto, *Polymer* **2006**, *47*, 5350.
- [55] M. Knite, A. Linarts, K. Ozols, V. Tupureina, I. Stalte, L. Lapcinskis, *Colloid. Surfaces A* **2017**, *526*, 8.
- [56] G. Cai, J. Wang, K. Qian, J. Chen, S. Li, P. S. Lee, *Adv. Sci.* **2017**, *4*, 1600190.
- [57] R. Pech-Pisté, M. Cen-Puc, A. Balam, A. May-Pat, F. Avilés, *Mater. Today Commun.* **2020**, *25*, 101472.
- [58] Y. Huang, M. Zhong, Y. Huang, M. Zhu, Z. Pei, Z. Wang, Q. Xue, X. Xie, C. Zhi, *Nat. Commun.* **2015**, *6*, 10310.
- [59] Y. Yue, N. Liu, Y. Ma, S. Wang, W. Liu, C. Luo, H. Zhang, F. Cheng, J. Rao, X. Hu, J. Su, Y. Gao, *ACS Nano* **2018**, *12*, 4224.
- [60] M. F. El-Kady, R. B. Kaner, *Nat. Commun.* **2013**, *4*, 1475.